Ultralow-loss integrated photonics enables bright, narrow-band, photon-pair sources

Ruiyang Chen,[1,2] Yi-Han Luo,[2,*] Jinbao Long,[2] Baoqi Shi,[2,3] Chen Shen,[2,4] and Junqiu Liu[2,5,†]

[1]*Shenzhen Institute for Quantum Science and Engineering, Southern University of Science and Technology, Shenzhen 518055, China*

[2]*International Quantum Academy, Shenzhen 518048, China*

[3]*Department of Optics and Optical Engineering, University of Science and Technology of China, Hefei, Anhui 230026, China*

[4]*Qaleido Photonics, Shenzhen 518048, China*

[5]*Hefei National Laboratory, University of Science and Technology of China, Hefei 230088, China*

Photon-pair sources are critical building blocks for photonic quantum systems. Leveraging Kerr nonlinearity and cavity-enhanced spontaneous four-wave mixing, chip-scale photon-pair sources can be created using microresonators built on photonic integrated circuit. For practical applications, a high microresonator quality factor Q is mandatory to magnify photon-pair sources' brightness and reduce their linewidth. The former is proportional to Q^4, while the latter is inversely proportional to Q. Here, we demonstrate an integrated, microresonator-based, narrow-band photon-pair source. The integrated microresonator, made of silicon nitride and fabricated using a standard CMOS foundry process, features ultralow loss down to 3 dB/m and intrinsic Q factor exceeding 10^7. The photon-pair source has brightness of 1.17×10^9 Hz/mW^2/GHz and linewidth of 25.9 MHz, both of which are record values for silicon-photonics-based quantum light source. It further enables a heralded single-photon source with heralded second-order correlation $g^{(2)}_{\mathrm{h}}(0) = 0.0037(5)$, as well as a energy-time entanglement source with a raw visibility of 0.973(9). Our work evidences the global potential of ultralow-loss integrated photonics to create novel quantum light sources and circuits, catalyzing efficient, compact and robust interfaces to quantum communication and networks.

Quantum science and technology have revolutionized our information society by offering a new paradigm to generate, transmit and process information. Photons – travelling at 3×10^8 m/s and free from decoherence – are irreplaceable carriers of quantum information[1,2]. Photons offer unrivalled coherence and immunity to perturbation for quantum computation[3–5], and have been ubiquitously used in quantum communication[6–10]. Currently, an emerging trend is to realize quantum information processing using photonic integrated circuit (PIC), which features small size, weight, and power consumption[11–13]. In addition, PIC-based quantum chips can be manufactured with large volume and low cost using established CMOS foundries. Indeed, in the last decade, integrated photonics has enabled increasingly diverse applications on quantum states manipulation[14,15], quantum key distribution[16], quantum networks[17], and quantum frequency conversion[18,19].

For photonic quantum systems, photon-pair sources are key building blocks. Particularly, narrow-band photon-pair sources are essential for long-distance quantum communication using quantum repeaters[20,21]. Here the narrow bandwidth is critical, as it must match the natural linewidth of atomic transition to ensure efficient photon-atom interface. Meanwhile, narrow-band photon-pair sources suffer minimum distortion from chromatic dispersion when transmitting over fibers. Moreover, a narrow band boosts the brightness (i.e. photon flux rate) of photon-pair sources, an equally central parameter for practical applications.

To build narrow-band photon-pair sources, nonlinear optical microresonators are particularly useful[22,23]. Compared to the methods using cavity-enhanced spontaneous parametric down-conversion (SPDC) with bulky crystals[24,25] or using atomic transition[26,27], optical microresonators are small, compact and robust. By leveraging the resonant nature for intracavity power enhancement, optical microresonators can offer exaggerated nonlinear effects, and have already been extensively used for optical frequency comb generation[28,29] and wideband frequency translation[30,31].

Previously, using microresonators on silicon PIC, photon-pair sources have achieved brightness of 1.6×10^8 Hz/mW^2/GHz and bandwidth of ~ 2 GHz[32]. The latter, due to the high optical loss (typically > 1 dB/cm) of silicon waveguides, is overwhelmingly larger than the natural linewidth of atomic transition (~ 10 MHz). The quest for even lower optical loss in PIC has motivated the rising and quick maturing of silicon nitride (Si_3N_4) integrated photonics. Integrated waveguides based on Si_3N_4 feature ultralow optical loss down to 1 dB/m[33] and tailorable dispersion[34], and have become the leading platform for nonlinear photonics[35,36], narrow-linewidth lasers[37,38], and linear networks[39,40] etc. Indeed, Si_3N_4 has unleashed new capability for on-chip photonic quantum information processing[41–47].

Here, we report a microresonator-based photon-pair source using ultralow-loss Si_3N_4 integrated photonics. The photon pairs are generated via cavity-enhanced spontaneous four-wave mixing (SFWM) in the optical microresonator[48,49], as the principle shown in Fig. 1a. In the presence of the microresonator's resonance grid, all the photons exist from the resonances of frequency $\omega(\mu)/2\pi$, where μ denotes the resonance mode index.

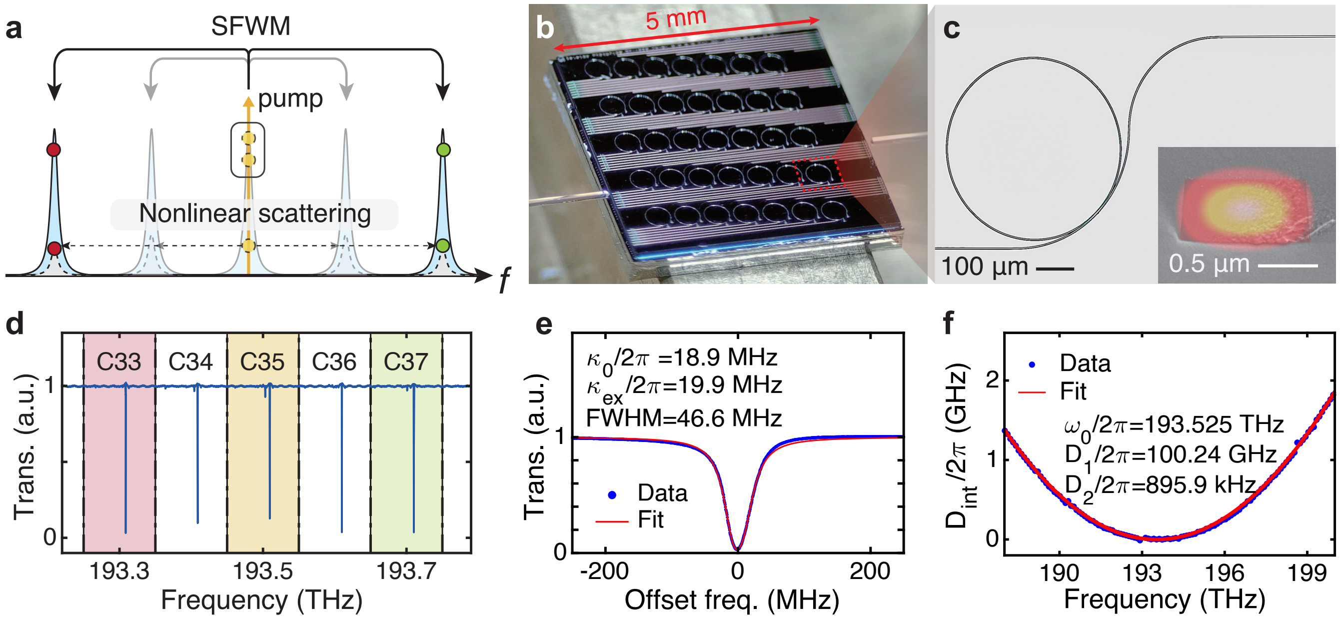

Figure 1. **Principle and characterization of integrated Si_3N_4 microresonators**. **a**. The principle of cavity-enhanced SFWM in an optical microresonator. Two pump photons annihilate, creating a pair of signal and idler photons aligned with the resonance grid. Meanwhile, nonlinear scattering process can incoherently transfer pump photons to other modes. **b**. Photo of the Si_3N_4 chip containing tens of microresonators. Lensed fibers are used for fiber-chip light coupling. **c**. Optical microscope image showing the layout of a 100-GHz-FSR microresonator. The inset presents the SEM image of the Si_3N_4 waveguide's cross section, superposed with the simulated TE_{00} optical mode. **d**. A segment of microresonator transmission spectrum, where the pump/signal/idler mode locates in C35/C37/C33. **e**. Resonance profile in C33 with a Lorentzian fit. **f**. Measured microresonator dispersion profile fitted with Eq. 1.

A continuous-wave (CW) laser of frequency $\omega(\mu_\mathrm{p})/2\pi$ is used to pump the microresonator. Via SFWM, two pump photons annihilate, creating a pair of signal and idler photons of frequency $\omega(\mu_\mathrm{s})/2\pi$ and $\omega(\mu_\mathrm{i})/2\pi$. The subscript p/s/i corresponds to the pump/signal/idler mode. In this process, the phase matching condition is automatically satisfied given $2\mu_\mathrm{p} = \mu_\mathrm{s} + \mu_\mathrm{i}$. The energy conservation $2\omega(\mu_\mathrm{p}) = \omega(\mu_\mathrm{s}) + \omega(\mu_\mathrm{i})$ requires anomalous (negative) group-velocity dispersion (GVD). A weak GVD is beneficial for a locally equidistant resonance grid. Additionally, strong optical confinement in the waveguides enhances intra-cavity electric field intensity, further facilitating SFWM.

Microresonator characterization. To satisfy these requirements, we design and fabricate integrated Si_3N_4 microresonators using a deep-ultraviolet (DUV) subtractive process on 6-inch wafers[50]. Figure 1b shows a photograph of one final Si_3N_4 chip of 5×5 mm^2 size containing tens of microresonators. Figure 1c shows the microresonator's layout under an optical microscope. The Si_3N_4 microresonators are formed with waveguides of 810-nm thickness and 2.4-μm width. The free spectral range (FSR) of the microresonators is 100 GHz. Figure 1c inset shows the scanning electron microscope (SEM) image of the waveguide's cross-section, together with the simulated optical field distribution of the fundamental transverse-electric (TE_{00}) mode. It is apparent that the waveguide geometry enables tight optical confinement. The gap between the bus waveguide and the microring resonator is 300 nm for over-coupling[51]. A pulley-style coupler where the bus waveguide adiabatically approaches the microring is applied to ensure high coupling ideality[52].

We characterize the Si_3N_4 microresonator using a vector spectrum analyzer in the telecommunication band[53]. Here we study the TE_{00} mode that has anomalous GVD and lowest loss among all microresonator's spatial modes. A segment of the microresonator's transmission spectrum is shown in Fig. 1d, where the frequency axis is calibrated with a relative precision better than 500 kHz. Each resonance of the 100-GHz-FSR microresonator locates in one International Telecommunication Union (ITU) channel, which can be separated using a dense wavelength-division multiplexer (DWDM). We plot and fit these resonances to extract the central frequency $\omega/2\pi$, the intrinsic loss $\kappa_0/2\pi$, and the external coupling strength $\kappa_\mathrm{ex}/2\pi$[54]. As an example, the resonance profile in Channel 33 (C33) is shown in Fig. 1e, with marked $\kappa_0/2\pi$, $\kappa_\mathrm{ex}/2\pi$ and the full width at half minimum/maximum (FWHM). The intrinsic and loaded quality factors are calculated as $Q_0 = \omega/\kappa_0 = 1.02\times10^7$ and $Q = \omega/\kappa = 4.97\times10^6$, where $\kappa = \kappa_0 + \kappa_\mathrm{ex}$. The measured FWHM is larger than $\kappa/2\pi$ due to the presence of mode split[54] (see Note 1 in Supplementary Materials for more details).

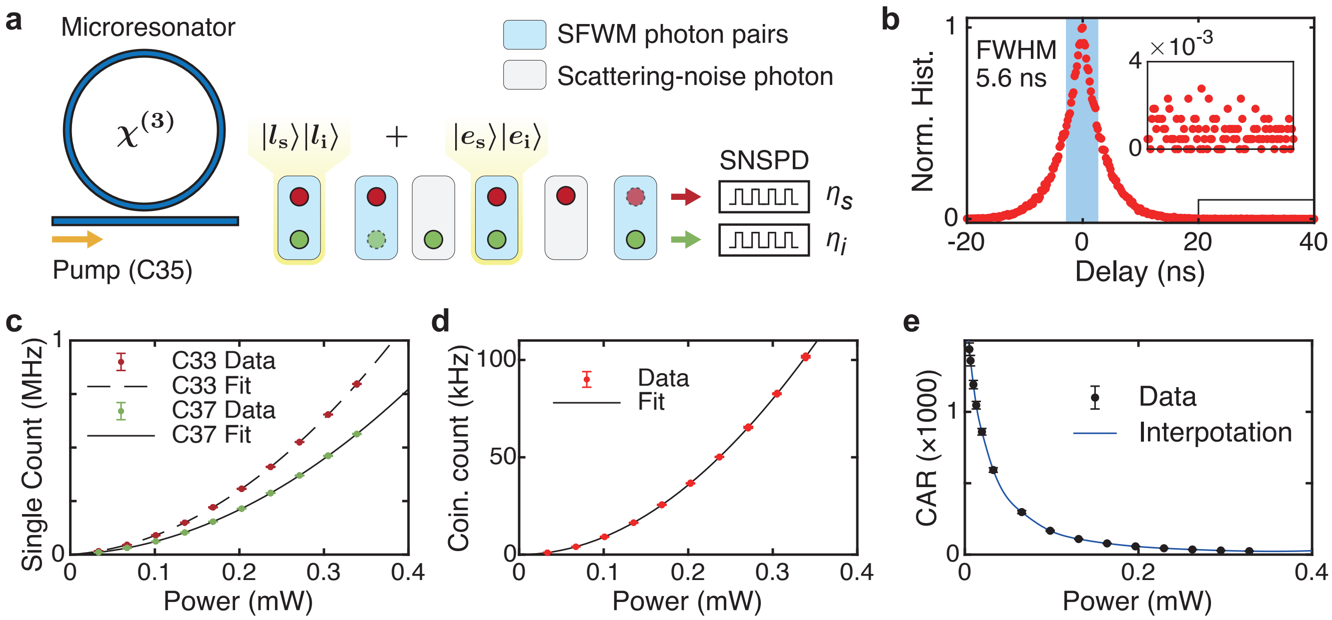

Figure 2. **Measurement of photon-pair brightness and coincidence-to-accidental ratio**. **a**. Schematic of the experiment. The Si_3N_4 microresonator is pumped with a CW laser whose frequency locates in C35. The generated photons are detected with SNSPDs and analyzed with a time-to-digital converter for brightness measurement. The photon pair created at an earlier moment, labeled as $|e_\mathrm{i}\rangle|e_\mathrm{s}\rangle$, is coherently superposed with the photon pair $|l_\mathrm{i}\rangle|l_\mathrm{s}\rangle$ generated later, resulting in a energy-time entanglement state $|\Psi\rangle = (|e_\mathrm{i}\rangle|e_\mathrm{s}\rangle + |l_\mathrm{i}\rangle|l_\mathrm{s}\rangle)/\sqrt{2}$. **b**. The measured two-photon correlation histogram normalized to its maximum. The bin width is 0.2 ns. The histogram is obtained with on-chip pump power of $P = 5.2$ μW and integration time of 3600 seconds. The FWHM of the peak at zero delay is 5.6 ns. The inset shows the zoom-in of background in the region far from the zero delay. **c**. The single count rates of signal (C37, green) and idler (C33, red) photons with different on-chip power, and their polynomial fit curves. **d**. The coincident count rate with different on-chip power, and its polynomial fit. The coincidence window width $\Delta t = 40$ ns is chosen. In panels (c, d), error bars are calculated as the standard deviation of ten independent measurements, which are however smaller than the size of the data points. **e**. The measured CAR with different on-chip power.

With the measured $\omega/2\pi$ for each resonance, the microresonator's dispersion is fitted with

$$D_\mathrm{int}(\mu) = \omega(\mu) - \omega(0) - D_1\mu = D_2\mu^2/2 + \mathcal{O}(\mu^3), \quad (1)$$

where $\omega(0)/2\pi$ is the pump resonance's frequency, $D_1/2\pi$ is the microresonator FSR, $D_2/2\pi$ is the GVD parameter. Higher-order dispersion terms are irrelevant in this work and thus neglected. The D_int profile and the extracted parameters are shown in Fig. 1f. The measured $D_2/2\pi = 895.9$ kHz is sufficiently small compared to resonance linewidth $\kappa/2\pi$, satisfying energy conservation.

Photon-pair generation. Experimentally we select the mode in Channel 35 (C35) as the pump mode. The signal and idler photons are generated in pairs in Channel 37 (C37) and C33, as illustrated in Fig. 1d. The photon-pair generation rate (PGR) via cavity-enhanced SFWM is $\alpha \propto \gamma^2 P^2 Q^3$, where γ is the effective Kerr coefficient and P is the on-chip pump power[48,49]. The photon-pair brightness is calculated as α/P^2 divided by the photon linewidth ($\sim 0.6\kappa/2\pi$, discussed later), thus is $\propto Q^4$. Consequently, a high-Q microresonator is extremely critical, as the photon-pair brightness is biquadratically magnified by the high Q.

We note that the correct measurement of photon-pair brightness poses several requirements. In the ideal case that only SFWM presents, the signal and idler photons are created strictly in pairs, marked as shaded blue in Fig. 2a. Considering the system efficiency $\eta_\mathrm{s/i}$, single count rate for the signal/idler photon on the superconducting-nanowire single-photon detectors (SNSPD) is $n_\mathrm{s/i} = \alpha\eta_\mathrm{s/i}$, resulting in the coincidence count rate $n_\mathrm{cc} = \alpha\eta_\mathrm{i}\eta_\mathrm{s}$. By measuring n_s, n_i and n_cc, the PGR is calculated as

$$\alpha = n_\mathrm{s} n_\mathrm{i}/n_\mathrm{cc} \quad (2)$$

However, in reality, nonlinear scattering process such as Raman scattering[55] occurs in microresonators. It can transfer the pump photons to other states, as the dashed arrows in Fig. 1a. The scattering-noise photons are unpaired and randomly mixed with the SFWM photon pairs, as shaded grey in Fig. 2a. Experimentally, scattering-noise photons cannot be distinguished from the SFWM photon pairs, as photons can be lost due to $\eta_\mathrm{s/i} < 1$, marked with dashed outline in Fig. 2a. Therefore, Eq. 2 fails and requires modification.

Considering that $\alpha \propto P^2$ and the generation rate of scattering-noise photons is $\alpha_\mathrm{sn} \propto P$, $n_\mathrm{s/i}$ and n_cc can be expressed as

$$n_{\mathrm{s/i}} = \eta_{\mathrm{s/i}} \left(aP^2 + b_{\mathrm{s/i}} P \right), \quad (3)$$

$$n_{\mathrm{cc}} - n_{\mathrm{acc}} = \eta_{\mathrm{i}} \eta_{\mathrm{s}} a P^2 + \mathcal{O}(P^3), \quad (4)$$

where n_{acc} is accidental coincidence count rate (discussed later), a is the PGR coefficient (i.e. $\alpha = aP^2$), and $b_{\mathrm{s/i}}$ is the coefficient corresponding to the scattering-noise photon generation. We note that, in the case that α and α_{sn} are comparable, n_{acc} contains higher-order terms proportional to P^3 and P^4, which should be included in the righthand of Eq. 4. Since the values of $n_{\mathrm{s/i}}$, n_{cc} and n_{acc} can be experimentally measured at different pump power P, $\eta_{\mathrm{s}} a$, $\eta_{\mathrm{i}} a$ and $\eta_{\mathrm{i}} \eta_{\mathrm{s}} a$ can be extracted via polynomial fit, allowing the calculation of a. More details on the fit formula can be found in Note 2 in Supplementary Materials.

The schematic of the experimental setup is shown in Fig. 2a, with more details found in Note 3 in Supplementary Materials. The photon-pair generation is evidenced by the two-photon correlation histogram shown in Fig. 2b, describing the distribution of the two-photon arrival time difference. The peak at the zero delay proves that the signal and idler photons are generated in pairs. The FWHM of the histogram peak is 5.6 ns. By summing up the bins within a window centered at zero delay and taking a specific width Δt, the coincidence count n_{cc} is obtained, while n_{acc} is obtained with the same Δt but far from the zero delay. We emphasize that, to obtain the correct brightness, Δt must be sufficiently large to account all the coincidence events. Otherwise the brightness will be overestimated. Here we take $\Delta t = 40$ ns for brightness measurement. More details can be found in Note 4 in Supplementary Materials.

The measured $n_{\mathrm{s/i}}$, n_{cc} and n_{acc} versus on-chip power P, together with their fit curves, are shown in Figs. 2d and 2e, respectively. The error bars are calculated as the standard deviation of ten independent measurements. Experimentally we obtain $a = 3.04 \times 10^7$ Hz/mW^2. Detailed fit results are found in Note 4 in Supplementary Materials. The generated photons' linewidth is estimated as $\delta\nu = 25.9$ MHz. The brightness is thus calculated as 1.17×10^9 Hz/mW^2/GHz. More details on the linewidth estimation are elaborated in Note 5 in Supplementary Materials.

In addition to the brightness, the noise level is equally important. As shown in Fig. 2b, for the region far outside the zero delay, the bin counts are not exactly zero, mainly due to the SFWM multi-photon excitation and the scattering noise. The coincidence-to-accidental ratio (CAR) is defined as $(n_{\mathrm{cc}}/n_{\mathrm{acc}} - 1)$. Figure 2c shows the measured CAR with $\Delta t = 5.6$ ns, i.e. the FWHM of the histogram peak in Fig. 2b. As the pump power P decreases, both the SFWM multi-photon excitation and the scattering noise decrease, resulting in a higher CAR. Experimentally, with $P = 5.2$ μW, we achieve $n_{\mathrm{cc}}/n_{\mathrm{acc}} - 1 = 1438 \pm 22$ with 3600 second integration. Meanwhile, the measured coincidence count rate is $n_{\mathrm{cc}} = 22$ Hz.

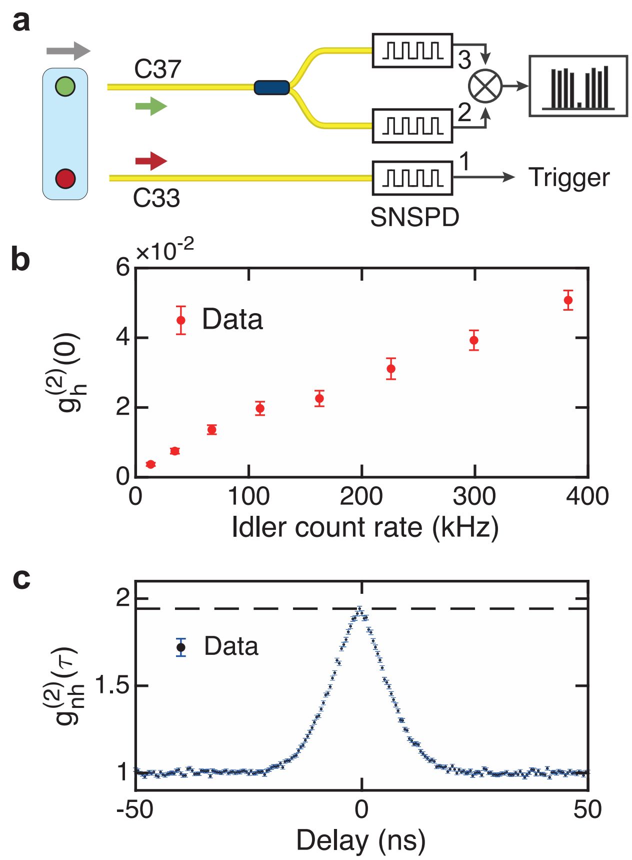

Figure 3. **Measurement of the second-order correlation**. **a**. Schematic of the experimental setup. The idler photons (C33, red) are directly detected with an SNSPD as trigger (marked as path 1). The signal photons (C37, green) are equally splitted and detected (marked as paths 2 and 3). The two-photon correlation histogram between paths 2 and 3 is measured with and without the path 1 clicking. **b**. Measured $g_{\mathrm{h}}^{(2)}(0)$ versus different idler photon count rate. **c**. Measured $g_{\mathrm{nh}}^{(2)}(\tau)$. The bin width is chosen as 0.5 ns. The maximum $g_{\mathrm{nh}}^{(2)}(\tau) = 1.942(14)$ is achieved at zero delay.

Second-order correlation. Photon-pair sources can be used as heralded single-photon sources. Once the SNSPD clicks upon the arrival of an idler photon, it heralds the existence of a signal photon. The photon anti-bunching can be observed with the heralded signal photons. To characterize the single-photon purity, a Hanbury Brown and Twiss (HBT) setup is utilized to measure the heralded second-order correlation $g_{\mathrm{h}}^{(2)}(0)$. As shown in Fig. 3a, the DWDM's C37 is equally splitted into two branches with marked path indices 2 and 3. Together with C33 of path index 1, the $g_{\mathrm{h}}^{(2)}(0)$ is calculated as $g_{\mathrm{h}}^{(2)}(0) = n_{123} n_1/(n_{12} n_{13})$, where n_1 is the single count rate, n_{12}, n_{13}, n_{123} are the coincidence count rates. Experimentally, we observe $g_{\mathrm{h}}^{(2)}(0) = 0.0037(5)$ at idler count rate $n_{\mathrm{s}} = 13.3$ kHz, with $P = 40$ μW and $\Delta t = 5.6$ ns. Due to the SFWM multi-pair excitation, $g_{\mathrm{h}}^{(2)}(0)$ in-

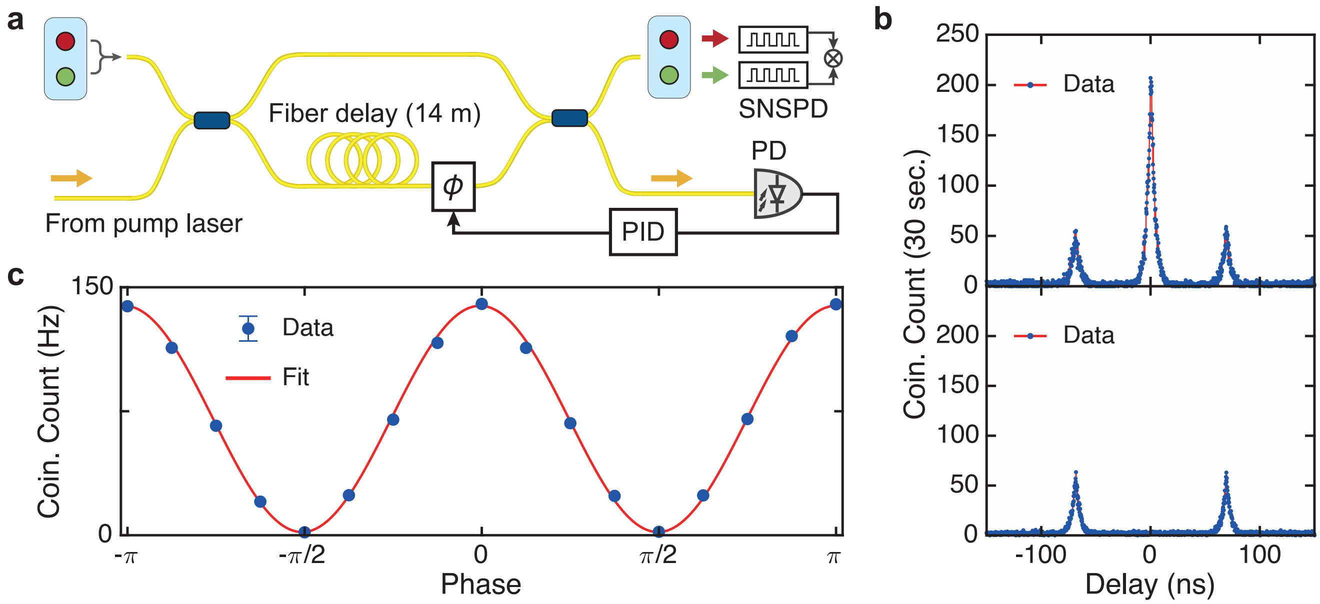

Figure 4. **Two-photon interference and energy-time entanglement**. **a**. Schematic of the experimental setup. To avoid single-photon interference, a 14-meter-long fiber link is used to introduce 69 ns delay. A portion of the pump laser is used to actively stabilize the phase difference between the two branches via controlling the added phase ϕ caused by the fiber stretcher. **b**. Two-photon correlation histogram. In the upper/lower panel, the peak at zero delay appears/vanishes due to constructive/destructive two-photon interference. **c**. Two-photon interference fringe. The sinusoidal fit shows a raw visibility of $V = 0.973(9)$ without background subtraction. Error bars are much smaller than the point size and thus are invisible.

creases with increasing P (thus n_i), as shown in Fig. 3b.

Next we characterize the spectral purity of the photon pairs by measuring the non-heralded second-order correlation $g^{(2)}_{\mathrm{nh}}(\tau)$[56]. Such measurement does not involve idler photons. The $g^{(2)}_{\mathrm{nh}}(\tau)$ histogram between paths 2 and 3 is shown in Fig. 3c. It is observed that $g^{(2)}_{\mathrm{nh}}(\tau) = 1.942(14)$ is reached at zero delay. It indicates that, a high multi-photon interference visibility between two independent photon-pair sources requires a narrow coincidence window[57]. This is mainly due to the strong spectral correlation of the photon pairs generated with the CW pump. The influence of the spectral correlation can be eliminated by introducing a dual interference scheme[58].

Two-photon interference visibility. Photon-pair sources can be regarded as narrow-band, energy-time entanglement light sources, which are advantageous for long-distance distribution due to their robustness against decoherence in optical fibers[59–61]. As shown in Fig. 2a, the photon pair created at an earlier moment, labeled as $|e_\mathrm{i}\rangle|e_\mathrm{s}\rangle$, is coherently superposed with the photon pair $|l_\mathrm{i}\rangle|l_\mathrm{s}\rangle$ generated later, where e/l denotes the earlier/later generated photon and the subscript s/i marks the signal/idler photon. Thus energy-time entangled photons $|\Psi\rangle = (|e_\mathrm{i}\rangle|e_\mathrm{s}\rangle + |l_\mathrm{i}\rangle|l_\mathrm{s}\rangle)/\sqrt{2}$ are created. To reveal the quantum interference, the two photons are projected along the state $|\phi\rangle = (|e\rangle + e^{i\phi}|l\rangle)/\sqrt{2}$ individually. The probability of measuring the state $|\Psi\rangle$ in $|\phi_\mathrm{i}\rangle|\phi_\mathrm{s}\rangle$ is calculated as $p = (1 + \cos 2\phi)/4$.

We use a folded Franson interferometer[62,63] to interfere two temporally separated photons. The setup is shown in Fig. 4a. The photons are equally splitted into two branches. In the lower branch, a 14-meter-long fiber link, corresponding to 69 ns delay, is introduced to avoid single-photon interference. A fiber stretcher is used to control the added phase ϕ. The two branches are then recombined and interfere. To suppress high-frequency phase fluctuation in the fiber due to ambient temperature fluctuation, we place the interferometer in a heat-insulated container. Additionally, a portion of the pump laser is used for active phase locking with a PID of 10 kHz bandwidth. The phase ϕ is varied by tuning the locking voltage and the PID's locking point.

The two-photon interference is evidenced by the two-photon correlation histogram shown in Fig. 4b. The central peak is post-selected, as it corresponds to the measurement of $|\Psi\rangle$. For $\phi = 0$, the central peak reaches maximum that is fourfold to the sidebands. When $\phi = \pi/2$, the central peak vanishes due to destructive interference. Detailed analysis is found in Note 6 in Supplementary Materials.

The measured two-photon interference is shown in Fig. 4c, where $\Delta t = 5.6$ ns is identical to that of CAR measurement. The coincidence count n_{cc} oscillates with a period of π. A sinusoidal fit using $n_{\mathrm{cc}} = 0.5N[1 + V\cos(\phi)]$ is applied to extract a raw visibility $V = 0.973(9)$ at $P = 97$ μW pump power, well above 0.707 and thus violating Clauser–Horne–Shimony–Holt (CHSH) inequality[64]. Due to the scattering noise, the background of the histogram in Fig. 4b is much larger than that of a crystal-based photon-pair source[65]. The background can severely deteriorate the interference visibility. In our experiment, the background is calculated by averaging the bin values far from the peaks. By subtracting the averaged background, we obtain a visibility of $V = 0.995(9)$.

Conclusion and discussion. In summary, we have studied integrated, high-Q, Kerr-nonlinear microresonators for bright, narrow-band, photon-pair generation. Using an over-coupled microresonator on ultralow-loss Si_3N_4 PIC and fabricated with a standard CMOS-foundry process, we realize a photon-pair source with brightness exceeding 1.17×10^9 Hz/mW^2/GHz and bandwidth below 25.9 MHz, both of which are record values for silicon-photonics-based quantum light sources. Moreover we achieve a CAR of $n_{\mathrm{cc}}/n_{\mathrm{acc}}-1 = 1438\pm22$, a heralded second-order correlation of $g_{\mathrm{h}}^{(2)}(0) = 0.0037(5)$, and a raw two-photon interference visibility of $V = 0.973(9)$. A comparison of integrated quantum light sources using microresonators is presented in Note 7 in Supplementary Materials.

Since the optical loss of our Si_3N_4 waveguides is far above the material limit of absorption loss[33,66], there is major space to further improve the microresonator Q factors by optimizing the material growth and fabrication process. Consequently, the brightness ($\propto Q^4$) can well exceed the best performance of recently developed highly nonlinear AlGaAs-on-insulator microresonators[67,68]. Combined with the wide transparency window of Si_3N_4 and broadband dispersion engineering, photon-pair generation from the visible to mid-infrared can be envisaged, paving the way to interfacing integrated photonics with a variety of quantum devices.

Acknowledgments: We thank Yuan Cao and Hui-Nan Wu for the fruitful discussion on Franson interferometer phase locking, Yun-Ru Fan for the suggestion on the energy-time entanglement measurement, and Shuyi Li for the suggestion on second-order correlation measurement. J. Liu acknowledges support from the National Natural Science Foundation of China (Grant No.12261131503), Innovation Program for Quantum Science and Technology (2023ZD0301500), Shenzhen-Hong Kong Cooperation Zone for Technology and Innovation (HZQB-KCZYB2020050), and from the Guangdong Provincial Key Laboratory (2019B121203002). Y.-H L. acknowledges support from the China Postdoctoral Science Foundation (Grant No. 2022M721482). The silicon nitride chips were fabricated by Qaleido Photonics. R. C. and Y.-H. L. contributed equally to this work.

Author contributions: Y.-H. L. and J. Liu conceived the experiment. R. C. and Y.-H. L. built the experimental setup, assisted with J. Long. S. C. fabricated the Si_3N_4 chip device. B. S. characterized the Si_3N_4 chip device. R. C., Y.-H. L. and J. Liu analyzed the data and prepared the manuscript with input from others. J. Liu supervised the project.

Conflict of interest: The authors declare no conflicts of interest.

Data Availability Statement: The code and data used to produce the plots within this work will be released on the repository `Zenodo` upon publication of this preprint.

* luoyh@iqasz.cn
† liujq@iqasz.cn

[1] J.-W. Pan, Z.-B. Chen, C.-Y. Lu, H. Weinfurter, A. Zeilinger, and M. Żukowski, Rev. Mod. Phys. **84**, 777 (2012).
[2] J. L. O'Brien, A. Furusawa, and J. Vučković, Nat. Photon. **3**, 687 (2009).
[3] H. Wang, J. Qin, X. Ding, M.-C. Chen, S. Chen, X. You, Y.-M. He, X. Jiang, L. You, Z. Wang, *et al.*, Phys. Rev. Lett. **123**, 250503 (2019).
[4] H.-S. Zhong, H. Wang, Y.-H. Deng, M.-C. Chen, L.-C. Peng, Y.-H. Luo, J. Qin, D. Wu, X. Ding, Y. Hu, *et al.*, Science **370**, 1460 (2020).
[5] L. S. Madsen, F. Laudenbach, M. F. Askarani, F. Rortais, T. Vincent, J. F. Bulmer, F. M. Miatto, L. Neuhaus, L. G. Helt, M. J. Collins, *et al.*, Nature **606**, 75 (2022).
[6] H. J. Kimble, Nature **453**, 1023 (2008).
[7] D. Bouwmeester, J.-W. Pan, K. Mattle, M. Eibl, H. Weinfurter, and A. Zeilinger, Nature **390**, 575 (1997).
[8] H.-K. Lo, M. Curty, and K. Tamaki, Nat. Photonics **8**, 595 (2014).
[9] Y.-A. Chen, Q. Zhang, T.-Y. Chen, W.-Q. Cai, S.-K. Liao, J. Zhang, K. Chen, J. Yin, J.-G. Ren, Z. Chen, *et al.*, Nature **589**, 214 (2021).
[10] C.-Y. Lu, Y. Cao, C.-Z. Peng, and J.-W. Pan, Rev. Mod. Phys. **94**, 035001 (2022).
[11] J. Wang, F. Sciarrino, A. Laing, and M. G. Thompson, Nature Photonics **14**, 273 (2020).
[12] A. W. Elshaari, W. Pernice, K. Srinivasan, O. Benson, and V. Zwiller, Nature Photonics **14**, 285 (2020).
[13] E. Pelucchi, G. Fagas, I. Aharonovich, D. Englund, E. Figueroa, Q. Gong, H. Hannes, J. Liu, C.-Y. Lu, N. Matsuda, J.-W. Pan, F. Schreck, F. Sciarrino, C. Silberhorn, J. Wang, and K. D. Jöns, Nature Reviews Physics **4**, 194 (2022).
[14] C. Vigliar, S. Paesani, Y. Ding, J. C. Adcock, J. Wang, S. Morley-Short, D. Bacco, L. K. Oxenløwe, M. G. Thompson, J. G. Rarity, *et al.*, Nat. Phys. **17**, 1137 (2021).
[15] J. Bao, Z. Fu, T. Pramanik, J. Mao, Y. Chi, Y. Cao, C. Zhai, Y. Mao, T. Dai, X. Chen, *et al.*, Nat. Photonics **17**, 573 (2023).
[16] P. Sibson, C. Erven, M. Godfrey, S. Miki, T. Yamashita, M. Fujiwara, M. Sasaki, H. Terai, M. G. Tanner, C. M. Natarajan, *et al.*, Nat. Commun. **8**, 13984 (2017).
[17] Y. Zheng, C. Zhai, D. Liu, J. Mao, X. Chen, T. Dai, J. Huang, J. Bao, Z. Fu, Y. Tong, *et al.*, Science **381**, 221 (2023).
[18] J. Holzgrafe, N. Sinclair, D. Zhu, A. Shams-Ansari, M. Colangelo, Y. Hu, M. Zhang, K. K. Berggren, and M. Lončar, Optica **7**, 1714 (2020).
[19] M. J. Weaver, P. Duivestein, A. C. Bernasconi, S. Scharmer, M. Lemang, T. C. v. Thiel, F. Hijazi, B. Hensen, S. Gröblacher, and R. Stockill, Nat. Nanotechnol. **19**, 166 (2024).
[20] N. Gisin and R. Thew, Nat. Photonics **1**, 165 (2007).
[21] A. I. Lvovsky, B. C. Sanders, and W. Tittel, Nat. Photonics **3**, 706 (2009).
[22] K. J. Vahala, Nature **424**, 839 (2003).

[23] J. D. Gómez, R. R. Alarcón, M. G. Robles, P. T. Ramírez, G. R. Becerra, E. Ortíz-Ricardo, and R. Salas-Montiel, Optics Letters **49**, 1860 (2024).
[24] Z. Y. Ou and Y. J. Lu, Phys. Rev. Lett. **83**, 2556 (1999).
[25] X.-H. Bao, Y. Qian, J. Yang, H. Zhang, Z.-B. Chen, T. Yang, and J.-W. Pan, Phys. Rev. Lett. **101**, 190501 (2008).
[26] V. Balić, D. A. Braje, P. Kolchin, G. Yin, and S. E. Harris, Phys. Rev. Lett. **94**, 183601 (2005).
[27] C. Shu, P. Chen, T. K. A. Chow, L. Zhu, Y. Xiao, M. Loy, and S. Du, Nat. Commun. **7**, 12783 (2016).
[28] T. J. Kippenberg, A. L. Gaeta, M. Lipson, and M. L. Gorodetsky, Science **361**, eaan8083 (2018).
[29] M. Kues, C. Reimer, J. M. Lukens, W. J. Munro, A. M. Weiner, D. J. Moss, and R. Morandotti, Nature Photonics **13**, 170 (2019).
[30] Q. Li, M. Davanço, and K. Srinivasan, Nature Photonics **10**, 406 (2016).
[31] X. Lu, G. Moille, Q. Li, D. A. Westly, A. Singh, A. Rao, S.-P. Yu, T. C. Briles, S. B. Papp, and K. Srinivasan, Nature Photonics **13**, 593 (2019).
[32] C. Ma, X. Wang, V. Anant, A. D. Beyer, M. D. Shaw, and S. Mookherjea, Opt. Express **25**, 32995 (2017).
[33] J. Liu, G. Huang, R. N. Wang, J. He, A. S. Raja, T. Liu, N. J. Engelsen, and T. J. Kippenberg, Nature Communications **12**, 2236 (2021).
[34] Y. Okawachi, M. R. E. Lamont, K. Luke, D. O. Carvalho, M. Yu, M. Lipson, and A. L. Gaeta, Opt. Lett. **39**, 3535 (2014).
[35] D. J. Moss, R. Morandotti, A. L. Gaeta, and M. Lipson, Nature Photonics **7**, 597 (2013).
[36] A. L. Gaeta, M. Lipson, and T. J. Kippenberg, Nature Photonics **13**, 158 (2019).
[37] W. Jin, Q.-F. Yang, L. Chang, B. Shen, H. Wang, M. A. Leal, L. Wu, M. Gao, A. Feshali, M. Paniccia, K. J. Vahala, and J. E. Bowers, Nature Photonics **15**, 346 (2021).
[38] C. Xiang, W. Jin, and J. E. Bowers, Photon. Res. **10**, A82 (2022).
[39] C. Taballione, T. A. Wolterink, J. Lugani, A. Eckstein, B. A. Bell, R. Grootjans, I. Visscher, D. Geskus, C. G. Roeloffzen, J. J. Renema, *et al.*, Opt. Express **27**, 26842 (2019).
[40] J. M. Arrazola, V. Bergholm, K. Brádler, T. R. Bromley, M. J. Collins, I. Dhand, A. Fumagalli, T. Gerrits, A. Goussev, L. G. Helt, J. Hundal, T. Isacsson, R. B. Israel, J. Izaac, S. Jahangiri, R. Janik, N. Killoran, S. P. Kumar, J. Lavoie, A. E. Lita, D. H. Mahler, M. Menotti, B. Morrison, S. W. Nam, L. Neuhaus, H. Y. Qi, N. Quesada, A. Repingon, K. K. Sabapathy, M. Schuld, D. Su, J. Swinarton, A. Száva, K. Tan, P. Tan, V. D. Vaidya, Z. Vernon, Z. Zabaneh, and Y. Zhang, Nature **591**, 54 (2021).
[41] S. Ramelow, A. Farsi, S. Clemmen, D. Orquiza, K. Luke, M. Lipson, and A. L. Gaeta, "Silicon-nitride platform for narrowband entangled photon generation," (2015), arXiv:1508.04358 [quant-ph].
[42] X. Lu, Q. Li, D. A. Westly, G. Moille, A. Singh, V. Anant, and K. Srinivasan, Nature Physics **15**, 373 (2019).
[43] F. Samara, A. Martin, C. Autebert, M. Karpov, T. J. Kippenberg, H. Zbinden, and R. Thew, Opt. Express **27**, 19309 (2019).
[44] F. Samara, N. Maring, A. Martin, A. S. Raja, T. J. Kippenberg, H. Zbinden, and R. Thew, Quantum Sci. Technol. **6**, 045024 (2021).
[45] K. Wu, Q. Zhang, and A. W. Poon, Opt. Express **29**, 24750 (2021).
[46] Y. Fan, C. Lyu, C. Yuan, G. Deng, Z. Zhou, Y. Geng, H. Song, Y. Wang, Y. Zhang, R. Jin, H. Zhou, L. You, Z. Wang, G. Guo, and Q. Zhou, Laser Photonics Rev. , 2300172 (2023).
[47] W. Wen, W. Yan, C. Lu, L. Lu, X. Wu, Y. Lu, S. Zhu, and X.-S. Ma, Phys. Rev. Appl. **20**, 064032 (2023).
[48] L. G. Helt, Z. Yang, M. Liscidini, and J. E. Sipe, Opt. Lett. **35**, 3006 (2010).
[49] K.-H. Luo, H. Herrmann, S. Krapick, B. Brecht, R. Ricken, V. Quiring, H. Suche, W. Sohler, and C. Silberhorn, New J. Phys. **17**, 073039 (2015).
[50] Z. Ye, H. Jia, Z. Huang, C. Shen, J. Long, B. Shi, Y.-H. Luo, L. Gao, W. Sun, H. Guo, J. He, and J. Liu, Photon. Res. **11**, 558 (2023).
[51] M. Cai, O. Painter, and K. J. Vahala, Phys. Rev. Lett. **85**, 74 (2000).
[52] M. H. P. Pfeiffer, J. Liu, M. Geiselmann, and T. J. Kippenberg, Phys. Rev. Applied **7**, 024026 (2017).
[53] Y.-H. Luo, B. Shi, W. Sun, R. Chen, S. Huang, Z. Wang, J. Long, C. Shen, Z. Ye, H. Guo, and J. Liu, Light Sci. Appl. **13**, 83 (2024).
[54] Q. Li, A. A. Eftekhar, Z. Xia, and A. Adibi, Phys. Rev. A **88**, 033816 (2013).
[55] M. Karpov, H. Guo, A. Kordts, V. Brasch, M. H. P. Pfeiffer, M. Zervas, M. Geiselmann, and T. J. Kippenberg, Phys. Rev. Lett. **116**, 103902 (2016).
[56] A. Christ, K. Laiho, A. Eckstein, K. N. Cassemiro, and C. Silberhorn, New J. Phys. **13**, 033027 (2011).
[57] Y.-P. Huang, J. B. Altepeter, and P. Kumar, Phys. Rev. A **82**, 043826 (2010).
[58] R.-Z. Liu, Y.-K. Qiao, H.-S. Zhong, Z.-X. Ge, H. Wang, T.-H. Chung, C.-Y. Lu, Y.-H. Huo, and J.-W. Pan, Sci. Bull. **68**, 807 (2023).
[59] I. Marcikic, H. De Riedmatten, W. Tittel, H. Zbinden, M. Legré, and N. Gisin, Phys. Rev. Lett. **93**, 180502 (2004).
[60] T. Inagaki, N. Matsuda, O. Tadanaga, M. Asobe, and H. Takesue, Opt. Express **21**, 23241 (2013).
[61] Y. Yu, F. Ma, X.-Y. Luo, B. Jing, P.-F. Sun, R.-Z. Fang, C.-W. Yang, H. Liu, M.-Y. Zheng, X.-P. Xie, *et al.*, Nature **578**, 240 (2020).
[62] J. D. Franson, Phys. Rev. Lett. **62**, 2205 (1989).
[63] Z. Y. Ou, X. Y. Zou, L. J. Wang, and L. Mandel, Phys. Rev. Lett. **65**, 321 (1990).
[64] J. F. Clauser, M. A. Horne, A. Shimony, and R. A. Holt, Physical review letters **23**, 880 (1969).
[65] H.-S. Zhong, Y. Li, W. Li, L.-C. Peng, Z.-E. Su, Y. Hu, Y.-M. He, X. Ding, W. Zhang, H. Li, *et al.*, Phys. Rev. Lett. **121**, 250505 (2018).
[66] M. Gao, Q.-F. Yang, Q.-X. Ji, H. Wang, L. Wu, B. Shen, J. Liu, G. Huang, L. Chang, W. Xie, S.-P. Yu, S. B. Papp, J. E. Bowers, T. J. Kippenberg, and K. J. Vahala, Nature Communications **13**, 3323 (2022).
[67] T. J. Steiner, J. E. Castro, L. Chang, Q. Dang, W. Xie, J. Norman, J. E. Bowers, and G. Moody, PRX Quantum **2**, 010337 (2021).
[68] L. Chang, W. Xie, H. Shu, Q.-F. Yang, B. Shen, A. Boes, J. D. Peters, W. Jin, C. Xiang, S. Liu, G. Moille, S.-P. Yu, X. Wang, K. Srinivasan, S. B. Papp, K. Vahala, and J. E. Bowers, Nature Communications **11**, 1331 (2020).